LETTER

doi:10.1038/nature09940

Spin crossover and iron-rich silicate melt in the Earth's deep mantle

Ryuichi Nomura[1,2], Haruka Ozawa[1,3], Shigehiko Tateno[1], Kei Hirose[1,3], John Hernlund[4], Shunsuke Muto[5], Hirofumi Ishii[6] & Nozomu Hiraoka[6]

A melt has greater volume than a silicate solid of the same composition. But this difference diminishes at high pressure, and the possibility that a melt sufficiently enriched in the heavy element iron might then become more dense than solids at the pressures in the interior of the Earth (and other terrestrial bodies) has long been a source of considerable speculation[1,2]. The occurrence of such dense silicate melts in the Earth's lowermost mantle would carry important consequences for its physical and chemical evolution and could provide a unifying model for explaining a variety of observed features in the core–mantle boundary region[3]. Recent theoretical calculations[4] combined with estimates of iron partitioning between (Mg,Fe)SiO_3 perovskite and melt at shallower mantle conditions[5–7] suggest that melt is more dense than solids at pressures in the Earth's deepest mantle, consistent with analysis of shockwave experiments[8]. Here we extend measurements of iron partitioning over the entire mantle pressure range, and find a precipitous change at pressures greater than ~76 GPa, resulting in strong iron enrichment in melts. Additional X-ray emission spectroscopy measurements on ($Mg_{0.95}Fe_{0.05}$)SiO_3 glass indicate a spin collapse around 70 GPa, suggesting that the observed change in iron partitioning could be explained by a spin crossover of iron (from high-spin to low-spin) in silicate melt. These results imply that (Mg,Fe)SiO_3 liquid becomes more dense than coexisting solid at ~1,800 km depth in the lower mantle. Soon after the Earth's formation, the heat dissipated by accretion and internal differentiation could have produced a dense melt layer up to ~1,000 km in thickness underneath the solid mantle. We also infer that (Mg,Fe)SiO_3 perovskite is on the liquidus at deep mantle conditions, and predict that fractional crystallization of dense magma would have evolved towards an iron-rich and silicon-poor composition, consistent with seismic inferences of structures in the core–mantle boundary region.

Our melting experiments were performed on samples with bulk composition ($Mg_{0.89}Fe_{0.11}$)$_2SiO_4$ at pressures from 20 to 159 GPa in a laser-heated diamond-anvil cell (DAC; Supplementary Table 1). The heating duration was short in order to avoid anomalous thermal diffusion (Supplementary Information), but this prevented us from measuring the melting temperature. Nevertheless, the upper and lower bounds of the temperature in our experiment are given by the liquidus temperature of Mg_2SiO_4 and the solidus temperature of natural peridotite, respectively (see Methods and Supplementary Fig. 1). Samples were recovered from the DAC and examined with a high-resolution field-emission-type electron probe micro-analyser (FE-EPMA). Recovered specimens exhibited a concentric texture that reflected the temperature distribution during heating (Fig. 1), which is similar to that observed in conventional multi-anvil experiments[5–7]. We consistently found a pocket at the hottest part of the sample that possessed non-stoichiometric composition, which we interpret as quenched partial melt. The (Mg+Fe)/Si molar ratio of this quenched melt increased with pressure, from 1.50 at 36 GPa to 2.56 at 159 GPa (Supplementary Fig. 2). The melt pocket was surrounded by a single-phase solid layer (ferropericlase or perovskite, depending on pressure), which we interpret to be

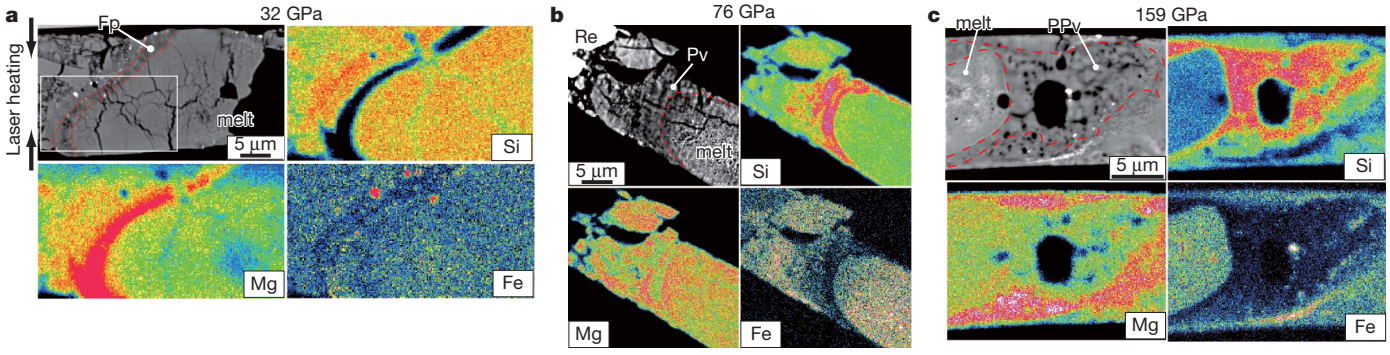

Figure 1 | Backscattered electron images and X-ray maps for Si, Mg and Fe for samples recovered from high-pressure melting experiments. **a**, At 32 GPa, when ferropericlase (Fp) is the liquidus phase; **b**, at 76 GPa, when perovskite (Pv) is the crystalline phase in contact with the quenched melt pocket; and **c**, at 159 GPa in the stability field of post-perovskite (PPv). Quenched melt was found at the centre of the sample, where the temperature was highest. Metallic iron was observed at the edge of the laser-heated area in all samples, where a strong temperature gradient existed[28]. It was also found in the melt pocket, but only above 36 GPa where the liquidus phase was perovskite or post-perovskite. Arrows in **a** represent the directions of the laser beams for heating. See Supplementary Information for the valence state of iron in the partial melt.

[1]Department of Earth and Planetary Sciences, Tokyo Institute of Technology, Meguro, Tokyo 152-8551, Japan. [2]Department of Earth and Planetary Sciences, University of Tokyo, Bunkyo, Tokyo 113-0033, Japan. [3]Institute for Research on Earth Evolution, Japan Agency for Marine-Earth Science and Technology, Yokosuka, Kanagawa 237-0061, Japan. [4]Department of Earth and Planetary Science, University of California, Berkeley, California 94720, USA. [5]Department of Materials, Physics and Energy Engineering, Nagoya University, Chikusa, Nagoya 464-8603, Japan. [6]National Synchrotron Radiation Research Center, Hsinchu 30076, Taiwan.

the phase that crystallizes first as temperature decreases (the liquidus phase)[5,7].

In this study, the liquidus phase was ferropericlase from 20 to 36 GPa and was subsequently replaced by perovskite at higher pressures (both were in contact with the melt pool at 36 GPa) (Fig. 1). Considering the difference in Mg/Si ratio of the samples[7], this is consistent with observations[5] of material with peridotite composition where the liquidus phase changes from ferropericlase to perovskite above 31 GPa. Although phase identification was not made, post-perovskite should have been formed in our experiments performed at 143 and 159 GPa. The change in liquidus phase from ferropericlase to perovskite at 36 GPa indicates that the eutectic melt composition becomes more Mg-rich at higher pressures. This is in agreement with the increase in (Mg+Fe)/Si molar ratio of partial melt with increasing pressure (Supplementary Fig. 2), although the partial melt composition also depends on the degree of melting.

The Fe-Mg distribution coefficient between perovskite/post-perovskite and melt, $K_D = ([Fe^{Pv}]/[Mg^{Pv}])/([Fe^{melt}]/[Mg^{melt}])$, was determined in the pressure range from 36 to 159 GPa (Fig. 2a), where perovskite/post-perovskite was the liquidus phase. Although the quenched melt pocket contained multiple valence states of iron (Fig. 1b, c), we consider that all Fe was present as Fe^{2+} at high temperature (see Supplementary Information). The obtained K_D values were approximately constant (at 0.22–0.29) below 73 GPa. These values are somewhat lower than previous determinations (~0.4) in Al-bearing peridotite bulk compositions[5–7] but are in good agreement with $K_D = 0.304 \pm 0.035$ at 25 GPa in Al-free peridotite material[6]. The high K_D in Al-bearing systems should be due to the high Fe^{3+} content of perovskite (see, for example, ref. 9). On the other hand, the value of K_D suddenly dropped to 0.07 ± 0.02 at 76 GPa (Fig. 2a). It then remained almost constant at 0.06–0.08 up to 159 GPa.

In order to explore the cause of strong Fe-enrichment in partial melt at pressures above 76 GPa, we collected the X-ray emission spectra of $(Mg_{0.95}Fe_{0.05})SiO_3$ glass at 300 K at increasing pressure, from 8 to 85 GPa (Fig. 3). At low pressures, the Fe Kβ′ satellite peak was clearly observed at 7,045 eV, showing the presence of high-spin Fe^{2+} in the glass sample. The satellite peak diminished somewhat at 59 GPa, and vanished at 77 GPa. This indicates a spin collapse in ferrous iron. Insofar as the glass is a good analogue for the liquid state, such a high-spin to low-spin crossover of iron may also occur in melt at a similar pressure range, thus providing an explanation for the measured jump in Fe-enrichment in partial melt (see, for example, refs 10, 11). Indeed, the pressure range of the spin crossover observed in our glass matches the pressure where K_D changed dramatically (Fig. 2a). Our melts had higher Mg/Si ratios and FeO contents than $(Mg_{0.95}Fe_{0.05})SiO_3$ glass; however, the calculated mean Mg–O and Si–O coordination numbers for Mg_2SiO_4 liquid[12] are very similar to those for $MgSiO_3$ liquid[13] at lower mantle pressures. Therefore, the spin crossover pressure, which depends on Mg/Fe–O coordination, would not shift significantly following a change in Mg/Si ratio in melt from 1 to 2. Theory[14,15] suggests that the Fe content does not change the pressure range of the spin crossover when the Fe concentration is small (less than ~20%), because Fe–Fe interactions are negligible. Multi-anvil experiments[16] have shown a very sharp change in Fe partitioning between perovskite and ferropericlase at the commencement of the spin crossover, which is compatible with the present observations.

A strong change in iron partitioning suggests that partial melt becomes more dense at depths below 1,800 km. We calculated the

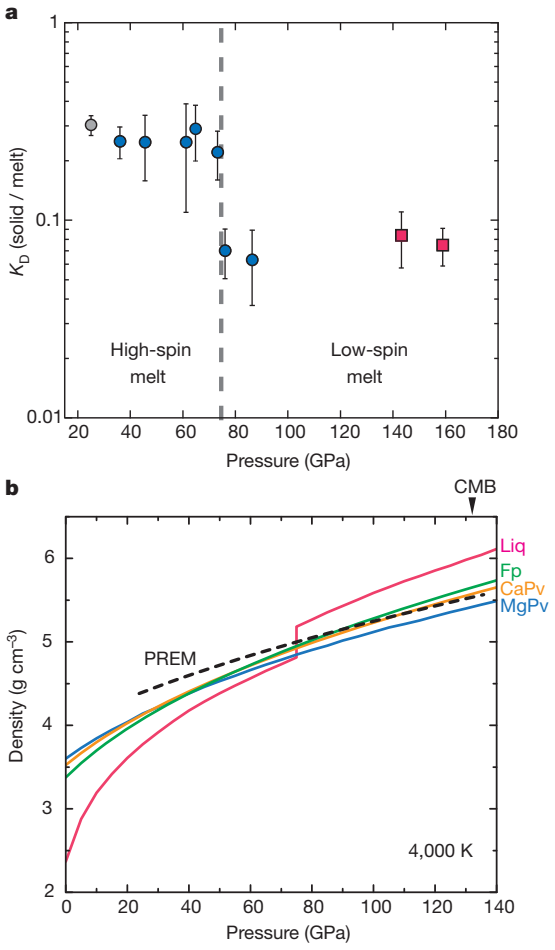

Figure 2 | Change in Fe-Mg distribution coefficient and calculated density profiles. a, $K_D = (Fe^{Pv}/Mg^{Pv})/(Fe^{melt}/Mg^{melt})$ between perovskite (blue circles) or post-perovskite (red squares) and melt; the values drop sharply at pressures above 76 GPa, probably due to the effect of the spin crossover of iron in silicate melt (see Fig. 3). Previous experimental datum obtained at 25 GPa using a multi-anvil apparatus is shown by a grey circle[6]. Error bars were estimated from uncertainties (1σ) in both solid and liquid compositions. **b**, Density of the $(Mg,Fe)SiO_3$ liquid coexisting with $(Mg_{0.92}Fe_{0.08})SiO_3$ perovskite calculated for 4,000 K using the newly obtained Fe-Mg partitioning data. Data for $(Mg_{0.86}Fe_{0.14})O$ ferropericlase[29], Ca-perovskite[30] and PREM[19] are also shown for comparison. Liq, liquid; Fp, ferro-periclase; CaPv, calcium silicate perovskite; MgPv, magnesium silicate perovskite.

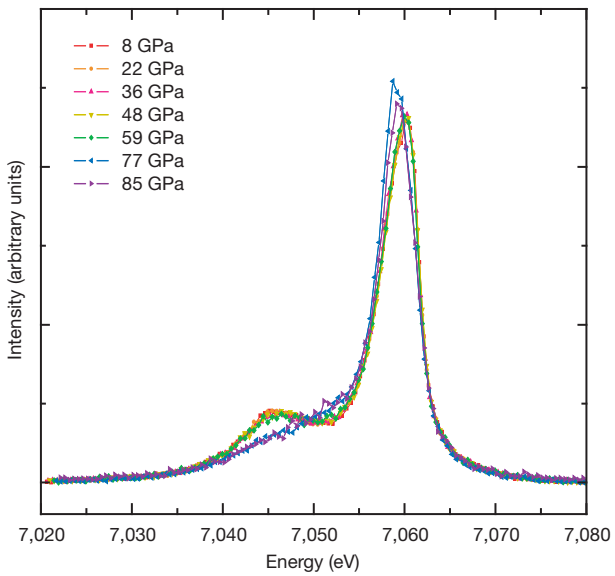

Figure 3 | Evolution of X-ray emission spectra of $(Mg_{0.95}Fe_{0.05})SiO_3$ glass with increasing pressure. Measurements were conducted at 300 K. All spectra are normalized to transmitted intensity, and shifted so that the weighted average of main (Kβ) plus satellite (Kβ′) emission lines is set to 7,058 eV. The satellite peak decreased slightly at 59 GPa and completely disappeared at 77 GPa, indicating the spin crossover of iron.

density of $(Mg,Fe)SiO_3$ liquid in equilibrium with $(Mg_{0.92}Fe_{0.08})SiO_3$ perovskite—a typical composition for pyrolitic lower mantle[16,17]—at 4,000 K as a function of pressure (Fig. 2b). For simplicity, we used $K_D = 0.25$ below 75 GPa and $K_D = 0.07$ at higher pressures. The molar volume of $MgSiO_3$ liquid was obtained by recent first principles calculations[4], and the effect of iron is assumed to be the same for liquid and solid (perovskite)[4,18]. Whereas $(Mg,Fe)SiO_3$ melt is buoyant compared to any of the typical lower-mantle minerals below 75 GPa, it suddenly becomes more dense at higher pressures. The difference from the preliminary reference Earth model (PREM)[19] reaches 8% at the base of the mantle. Partial melts obtained in the present experiments had a higher Mg/Si ratio than $MgSiO_3$ (Supplementary Fig. 2). According to previous shock-wave compression experiments[8], such high-(Mg+Fe)/Si melt is likely to be denser than the $(Mg,Fe)SiO_3$ melt considered above, suggesting that the density crossover between melt and solid may occur even at depths shallower than 1,800 km. Although details of the formation of melts at the base of the mantle are not yet clear, the present results provide a constraint on the plausible thickness of any stable melt layer of around 1,000 km (Fig. 4).

Labrosse *et al.*[3] have presented a model in which dense melts produced soon after Earth's formation comprised a potentially large 'basal magma ocean' (BMO), which underwent slow crystallization over billions of years, at a rate governed by relatively sluggish solid state convection in the overlying solid mantle. The present experimental results provide a new physical rationale for the gravitational stability of a BMO up to ~1,000 km thick underneath the solid mantle, and the maximum plausible thickness inferred above is broadly consistent with the BMO hypothesis. For example, a BMO of ~1,000 km thickness would comprise about one-quarter of the mantle's mass; fractional crystallization and sequestering of incompatible heat producing elements (for example, U, Th) in the residual liquid as the layer cools would therefore account for the 'missing' chondritic complement of these species expected to be sequestered in a reservoir inside the mantle[20]. The present results also allow us to make further predictions about the nature of the BMO and its chemical evolution through time.

As noted above, our results demonstrate that $(Mg,Fe)SiO_3$ perovskite is the first phase to crystallize from melts with a wide range of (Mg+Fe)/Si ratios; this is true even for Si-poor melt with $(Mg+Fe)/Si \approx 2.5$ at the conditions of the core–mantle boundary (Supplementary Fig. 2). This strongly suggests that an episode of perovskite crystallization might well characterize the majority of the freezing history of a BMO, with other phases such as (Mg,Fe)O magnesiowüstite only crystallizing relatively late. In addition, perovskite crystals forming in the BMO would have been relatively depleted in iron and floated to the top of magmas at depths greater than 1,800 km (Fig. 4), because of the small K_D value for Fe/Mg partitioning. As a consequence, we can predict that the residual magma would evolve towards a FeO-rich/SiO_2-poor composition (that is, near the composition of wüstite), becoming more dense with time and probably also retaining a variety of incompatible volatile species.

Evolution through fractional crystallization as described above would also have affected the composition of cumulates that formed from the BMO. In particular, cumulates should become more Fe-rich with time, and presumably more dense, as they crystallize from an increasingly Fe-rich magma. These dense cumulates themselves might eventually become stable against complete entrainment by mantle convection currents, and pile up at the base of the mantle to form thermo-chemical piles (Fig. 4). The accumulation of dense solid material, which is around 2–3% denser than average mantle and which comprises ~2% of the total mantle volume, can explain the presence of two large, low-shear-wave velocity provinces (LLSVPs) at the base of the mantle beneath the Pacific and Africa[21]; and the expected Fe-enriched composition of the dense material is consistent with the magnitude of these anomalies[22].

Larger degrees of crystallization in a BMO could also have left patches of dense residual mush in thin layers above the core–mantle boundary, which would explain the presence and seismic velocities of ultralow-velocity zones (ULVZs)[23]. Such material would be maintained at or near the solidus over geological timescales because the residual liquid would sequester incompatible species that in turn depress the melting temperature. Alternatively, late crystallization of wüstite-rich cumulates from the Fe-rich/Si-poor melt could have left behind a dense solid layer with seismic properties that may also be consistent with seismic inferences for ULVZ, even in the absence of melt[24]. The BMO model, together with the evolution of composition that we predict from our experiments, is compatible with both possibilities. Another possibility that might help to explain why ULVZs in

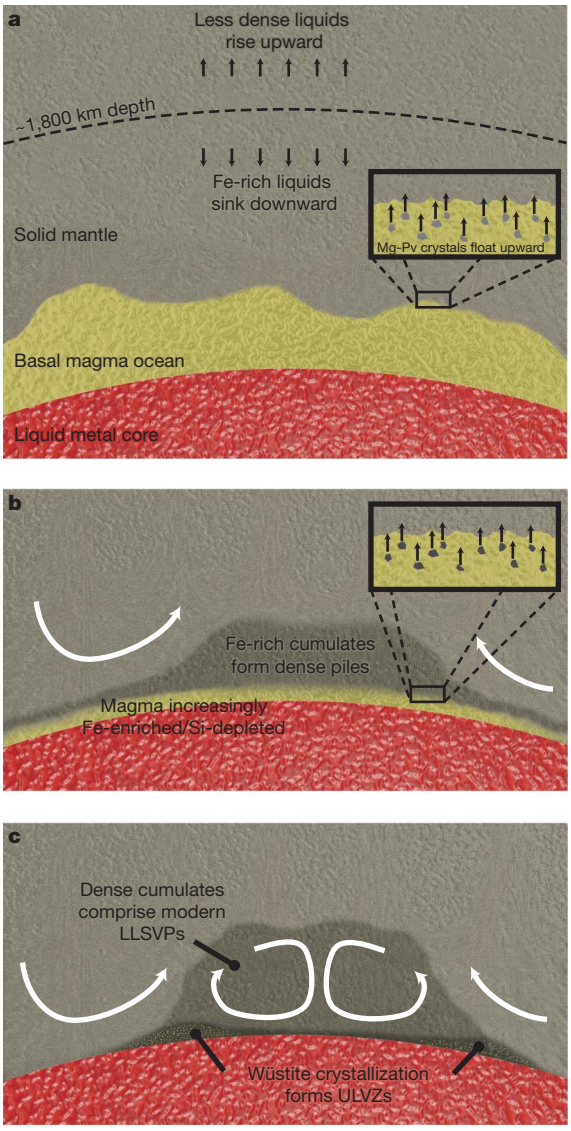

Figure 4 | Evolution and crystallization of dense melts in the deep mantle. **a**, During Earth's early history, any melts that form below ~1,800 km depth sink and accumulate at the base of the mantle, while any crystals that form owing to cooling of this dense magma will rise upward into the solid mantle. **b**, Fe-poor perovskite crystallization leaves a residual liquid enriched in FeO and depleted in SiO_2, and crystals forming from this evolved liquid may become dense enough to form thermo-chemical piles at the base of the solid mantle. **c**, The final stage of crystallization involves a composition close to wüstite, leaving behind a very dense thin layer that is consistent with the seismic properties inferred inside ULVZs. White arrows indicate schematic flow patterns in the convecting solid mantle.

different regions do not always exhibit the same seismic signatures[25] is that inside some ULVZs the interstitial melt has drained out, leaving a largely melt-free solid rock strongly enriched in wüstite. In other ULVZs, owing to different dynamical conditions in the surrounding mantle, continual stirring of the mushy residue by viscous coupling to flows in the overlying mantle might have prevented compaction of the rock and removal of melt[26]. The primary difference we would expect to observe between a melt-free, wüstite-rich ULVZ and a persistently mushy ULVZ would be the strength of the reduction in shear wave velocity, with a greater reduction inside mushy ULVZs[27].

METHODS SUMMARY

We loaded a platelet of $(Mg_{0.89}Fe_{0.11})_2SiO_4$ olivine starting material into the DAC together with argon pressure medium. After compression, the sample was heated by laser to induce melting. Subsequently it was recovered from the DAC and polished parallel to the compression axis. We obtained chemical compositions of the quenched liquid pool and the neighbouring solid phase (liquidus phase) from FE-EPMA analyses of these sections. In addition, several samples were further processed to a thin film and examined under a transmission electron microscope (TEM). The $Fe^{3+}/(Fe^{2+} + Fe^{3+})$ ratio of the quenched melt pocket was determined by electron energy-loss near-edge structure (ELNES) measurements. We also carried out the X-ray emission spectroscopy (XES) study of $(Mg_{0.95}Fe_{0.05})SiO_3$ glass in the DAC at high pressure and room temperature. The high-resolution spectra of the Fe Kβ line were collected through the cubic boron nitride + beryllium composite gasket, and indicate the change in the spin state of iron with increasing pressure.

Full Methods and any associated references are available in the online version of the paper at www.nature.com/nature.

Received 8 September 2010; accepted 16 February 2011.
Published online 24 April 2011.

1. Stolper, E., Walker, D., Hager, B. H. & Hays, J. F. Melt segregation from partially molten source regions: the importance of melt density and source region size. *J. Geophys. Res.* **86,** 6261–6271 (1981).
2. Agee, C. B. Crystal-liquid density inversions in terrestrial and lunar magmas. *Phys. Earth Planet. Inter.* **107,** 63–74 (1998).
3. Labrosse, S., Hernlund, J. W. & Coltice, N. A crystallizing dense magma ocean at the base of the Earth's mantle. *Nature* **450,** 866–869 (2007).
4. Stixrude, L. *et al.* Thermodynamics of silicate liquids in the deep Earth. *Earth Planet. Sci. Lett.* **278,** 226–232 (2009).
5. Ito, E., Kubo, A., Katsura, T. & Walter, M. J. Melting experiments of mantle materials under lower mantle conditions with implications for magma ocean differentiation. *Phys. Earth Planet. Inter.* **143–144,** 397–406 (2004).
6. Corgne, A. *et al.* Silicate perovskite-melt partitioning of trace elements and geochemical signature of a deep perovskitic reservoir. *Geochim. Cosmochim. Acta* **69,** 485–496 (2005).
7. Liebske, C. *et al.* Compositional effects on element partitioning between Mg-silicate perovskite and silicate melts. *Contrib. Mineral. Petrol.* **149,** 113–128 (2005).
8. Mosenfelder, J. L., Asimov, P. D. & Ahrens, T. J. Thermodynamic properties of Mg_2SiO_4 liquid at ultra-high pressures from shock measurements to 200 GPa on forsterite and wadsleyite. *J. Geophys. Res.* **112,** B06208, doi:10.1029/2006JB004364 (2007).
9. McCammon, C. Perovskite as a possible sink for ferric iron in the lower mantle. *Nature* **387,** 694–696 (1997).
10. Badro, J. *et al.* Iron partitioning in Earth's mantle: toward a deep lower mantle discontinuity. *Science* **300,** 789–791 (2003).
11. Auzende, A.-L. *et al.* Element partitioning between magnesium silicate perovskite and ferropericlase: new insights into bulk lower-mantle geochemistry. *Earth Planet. Sci. Lett.* **269,** 164–174 (2008).
12. de Koker, N. P., Stixrude, L. & Karki, B. B. Thermodynamics, structure, dynamics, and freezing of Mg_2SiO_4 liquid at high pressure. *Geochim. Cosmochim. Acta* **72,** 1427–1441 (2008).
13. Karki, B. B. First-principles molecular dynamics simulations of silicate melts: structural and dynamical properties. *Rev. Mineral. Geochem.* **71,** 355–389 (2010).
14. Tsuchiya, T., Wentzcovitch, R. M., da Silva, C. R. S. & de Gironcoli, S. Spin transition in magnesiowüstite in Earth's lower mantle. *Phys. Rev. Lett.* **96,** 198501 (2006).
15. Bengtson, A., Persson, K. & Morgan, D. Ab initio study of the composition dependence of the pressure-induced spin crossover in perovskite $(Mg_{1-x},Fe_x)SiO_3$. *Earth Planet. Sci. Lett.* **265,** 535–545 (2008).
16. Irifune, T. *et al.* Iron partitioning and density change of pyrolite in Earth's lower mantle. *Science* **327,** 193–195 (2010).
17. Hirose, K. Phase transition in pyrolitic mantle around 670-km depth: implications for upwelling of plumes from the lower mantle. *J. Geophys. Res.* **107,** 2078, doi:10.1029/2001JB000597 (2002).
18. Lundin, S. *et al.* Effect of Fe on the equation of state of mantle silicate perovskite over 1 Mbar. *Phys. Earth Planet. Inter.* **168,** 97–102 (2008).
19. Dziewonski, A. M. & Anderson, D. L. Preliminary reference Earth model. *Phys. Earth Planet. Inter.* **25,** 297–356 (1981).
20. Hofmann, A. W. Mantle geochemistry: the message from oceanic volcanism. *Nature* **385,** 219–229 (1997).
21. Hernlund, J. W. & Houser, C. On the distribution of seismic velocities in Earth's deep mantle. *Earth Planet. Sci. Lett.* **265,** 423–437 (2008).
22. Cobden, L. *et al.* Thermochemical interpretation of 1-D seismic data for the lower mantle: the significance of nonadiabatic thermal gradients and compositional heterogeneity. *J. Geophys. Res.* **114,** B11309, doi:10.1029/2008JB006262 (2009).
23. Williams, Q. & Garnero, E. J. Seismic evidence for partial melt at the base of Earth's mantle. *Science* **273,** 1528–1530 (1996).
24. Wicks, J. K., Jackson, J. M. & Sturhahn, W. Very low sound velocities in iron-rich (Mg,Fe)O: implications for the core-mantle boundary region. *Geophys. Res. Lett.* **37,** L15304, doi:10.1029/2010GL043689 (2010).
25. Thorne, M. S. & Garnero, E. J. Inferences on ultralow-velocity zone structure from a global analysis of SPdKS waves. *J. Geophys. Res.* **109,** B08301, doi:10.1029/2004JB003010 (2004).
26. Hernlund, J. W. & Jellinek, A. M. Dynamics and structure of a stirred partially molten ultralow velocity zone. *Earth Planet. Sci. Lett.* **296,** 1–8 (2010).
27. Hier-Majumder, S. Influence of contiguity on seismic velocities of partially molten aggregates. *J. Geophys. Res.* **113,** B12205, doi:10.1029/2008JB005662 (2008).
28. Fialin, M., Catillon, G. & Andrault, D. Disproportionation of Fe^{2+} in Al-free silicate perovskite in the laser heated diamond anvil cell as recorded by electron probe microanalysis of oxygen. *Phys. Chem. Miner.* **36,** 183–191 (2009).
29. Komabayashi, T. *et al.* High-temperature compression of ferropericlase and the effect of temperature on iron spin transition. *Earth Planet. Sci. Lett.* **297,** 691–699 (2010).
30. Ricolleau, A. *et al.* Density profile of pyrolite under the lower mantle conditions. *Geophys. Res. Lett.* **36,** L06302, doi:10.1029/2008GL036759 (2009).

Supplementary Information is linked to the online version of the paper at www.nature.com/nature.

Acknowledgements We thank R. Sinmyo for support with TEM analyses and K. Shimizu for preparing the glass sample. Discussion with R. Caracas and comments from D. Frost were helpful. C.-C. Chen is acknowledged for XES measurements at BL12XU Taiwan Beamline, SPring-8. Some of the melting experiments were conducted at BL10XU (SPring-8 proposal no. 2009B0087). J.H. was supported by the National Science Foundation (NSFEAR0855737).

Author Contributions R.N., H.O., S.T. and K.H. performed high-pressure experiments and chemical analyses. S.M. carried out the ELNES measurements. H.I. and N.H. supported the XES study at SPring-8. R.N., K.H. and J.H. wrote the paper. All authors discussed the results and commented on the manuscript.

Author Information Reprints and permissions information is available at www.nature.com/reprints. The authors declare no competing financial interests. Readers are welcome to comment on the online version of this article at www.nature.com/nature. Correspondence and requests for materials should be addressed to K.H. (kei@geo.titech.ac.jp).

METHODS

Melting experiments at high pressure. High-pressure and high-temperature conditions were generated using laser-heated diamond-anvil cell (DAC) techniques. $(Mg_{0.89}Fe_{0.11})_2SiO_4$ olivine from KLB-1 natural peridotite was used as a starting material[31]. The powdered sample was pressed into a disk with a typical thickness of 15–25 μm and was placed into a hole drilled at the centre of the rhenium gasket, which was pre-indented to a thickness of 25–40 μm. No additional metal absorber was used. Liquid argon was loaded cryogenically as a pressure medium. The sample was compressed with bevelled 120-μm and 150-μm, or flat 300-μm, culet diamond anvils, depending on a target pressure. Heating was performed with a fibre laser or a doughnut-mode Nd:YLF laser using a double-side heating technique that minimizes axial temperature gradients within the sample[32]. The laser spot size was about 20–30 μm on the sample.

The sample was heated for less than 1 s in order to avoid chemical segregation due to thermal diffusion under relatively large temperature gradient (see 'Attainment of chemical equilibrium' section in Supplementary Information). This heating duration was too short to allow accurate temperature measurement. Alternatively, we estimated the temperature in our experiment from the reported liquidus temperature of Mg_2SiO_4 (refs 8, 33) and the solidus temperature of natural peridotite[34], which give the upper and lower bounds, respectively (Supplementary Fig. 1). Pressure was determined from the Raman peak shift of the diamond anvil at 300 K after laser-heating[35]. Here we assumed that the pressure was higher by 20% at melting temperature than at 300 K due to a contribution of thermal pressure, which was estimated from the previous *in-situ* X-ray diffraction measurements[36]. The overall pressure uncertainty may be about ±10%.

Chemical analyses of recovered samples. After complete pressure release, the sample was recovered from the DAC and glued on a silicon wafer using polymeric resin. Subsequently it was polished parallel to the compression axis by an Ar ion beam using an Ion Slicer (JEOL EM-09100 IS)[37]. This method minimizes the damage of the sample surface, allowing us to observe microstructures within the extremely small sample. The section was examined by FE-EPMA (JEOL JXA-8500F) using an acceleration voltage of 10 kV and a beam current of 12 nA. We collected X-ray mappings for Si, Mg and Fe for each sample (Fig. 1 and Supplementary Figs 3 and 4). Chemical compositions of the quenched liquid pool and the neighbouring solid phase (ferropericlase, perovskite, or post-perovskite, depending on pressure) were obtained with defocused (5-μm size) and focused (<2-μm spatial resolution) beams, respectively (Supplementary Table 1). Synthetic wollastonite ($CaSiO_3$), periclase (MgO), and haematite (Fe_2O_3) were used as standards. In runs 21 and 24, however, the analyses of ferropericlase were contaminated by the melt pocket and were therefore estimated by subtracting the melt composition from the EPMA analyses until the SiO_2 content in ferropericlase becomes zero.

In addition, the samples in runs 17, 18 and 21 were further processed to a thin film by using an Ion Slicer and examined under a transmission electron microscope (TEM). For run 18, the $Fe^{3+}/(Fe^{2+} + Fe^{3+})$ ratio of the quenched melt pocket was determined by electron energy-loss near-edge structure (ELNES) spectroscopy measurements (Supplementary Fig. 5). The Fe $L_{2,3}$-edge ELNES spectra were collected by using a JEM-2100M with an Enfina1000 spectrometer at Nagoya University. The measurements were made with a dispersion of 0.1 eV per channel, a typical energy resolution of about 0.8 eV, and an integration time of 25–100 s. The spectra were recorded using a macroscript for the Gatan Digital Micrograph (which controls the spectrometer) that corrects for energy drifts during data accumulation. This avoids the problem of peak broadening that follows prolonged data accumulation[38]. The incident beam current was about 0.1 nA, and the fluence rate was about 50 e $Å^{-2}$ s^{-1}. The quantitative determination of the $Fe^{3+}/(Fe^{2+} + Fe^{3+})$ ratio is based on the white line intensities at the Fe $L_{2,3}$-edge, following the method described in ref. 39. The validity of the present analytical procedures was checked on a couple of silicate glass standards, whose $Fe^{3+}/(Fe^{2+} + Fe^{3+})$ ratios had been previously determined by Mössbauer spectroscopy measurements to be 0.38 and 0.83 (ref. 40). Our ELNES analyses determined the $Fe^{3+}/(Fe^{2+} + Fe^{3+})$ ratios for these glass samples to be 0.40 ± 0.02 and 0.79 ± 0.09. A systematic change in $Fe^{3+}/(Fe^{2+} + Fe^{3+})$ ratios was not found with increasing electron beam irradiation time, up to 100 s.

X-ray emission spectroscopy measurements. High resolution X-ray emission spectra (XES) of the Fe Kβ line were obtained for $(Mg_{0.95}Fe_{0.05})SiO_3$ glass at the BL12XU beamline of SPring-8 (ref. 41). The glass sample was prepared by quenching melt from 1,931 K in a CO_2-H_2 gas-mixing furnace. The oxygen fugacity in the high-temperature furnace was controlled to be slightly above the iron–wüstite buffer, in which all Fe was present as ferrous iron. The FE-EPMA analyses confirmed that the sample was glass without any quench-crystals and had a chemical composition of $(Mg_{0.95}Fe_{0.05})SiO_3$ as a consequence of partial loss of iron into the Pt basket that held the sample in the furnace. X-ray diffraction measurements also showed the starting material to be amorphous.

XES measurements were made at room temperature in the DAC with increasing pressure from 8 to 85 GPa (Fig. 3). We used a cubic boron nitride (inner) + beryllium (outer) composite gasket. The glass powder was loaded into a hole in the gasket, which was pre-indented to about 80 μm in thickness. In order to excite the sample through diamond, monochromatic X-rays at 11 keV were chosen as the incident beam. The incident X-ray beam was focused on and collimated to 15-μm size at the sample. A 1-m Rowland circle type spectrometer, equipped with 1-m spherical bent Ge(620) analyser, was used to acquire the emission spectra. These spectra were collected through the gasket in order to avoid a loss of intensity due to absorption by the diamond. The spectra covered the energy range from 7,020 to 7,080 eV with a resolution of 0.5 eV.

31. Takahashi, E. Melting of a dry peridotite KLB-1 up to 14 GPa: implications on the origin of peridotitic upper mantle. *J. Geophys. Res.* **91,** 9367–9382 (1986).
32. Shen, G., Mao, H. K. & Hemley, R. J. in *Advanced Materials '96* 149–152 (Proc. 3rd NIRIM International Symposium on Advanced Materials, 1996).
33. Presnall, D. C., Weng, Y.-H., Milholland, C. S. & Walter, M. J. Liquidus phase relations in the system MgO–$MgSiO_3$ at pressures up to 25 GPa — constraints on crystallization of a molten Hadean mantle. *Phys. Earth Planet. Inter.* **107,** 83–95 (1998).
34. Fiquet, G. *et al.* Melting of peridotite to140 gigapascals. *Science* **329,** 1516–1518 (2010).
35. Akahama, Y. & Kawamura, H. High pressure Raman spectroscopy of diamond anvils to 250 GPa: method for pressure determination in the multimegabar pressure range. *J. Appl. Phys.* **96,** 3748–3751 (2004).
36. Ozawa, H. *et al.* Experimental study of reaction between perovskite and molten iron to 146 GPa and implications for chemically distinct buoyant layer at the top of the core. *Phys. Chem. Miner.* **36,** 355–363 (2009).
37. Tateno, S., Sinmyo, R., Hirose, K. & Nishioka, H. The advanced ion-milling method for preparation of thin film using Ion Slicer: application to a sample recovered from diamond-anvil cell. *Rev. Sci. Instrum.* **80,** 013901 (2009).
38. Sasano, Y. & Muto, S. Energy-drift correction of electron energy-loss spectra from prolonged data accumulation of low SNR signals. *J. Electron Microsc.* **57,** 149–158 (2008).
39. van Aken, P. A., Liebscher, B. & Styrsa, V. J. Quantitative determination of iron oxidation states in minerals using Fe $L_{2,3}$-edge electron energy-loss near-edge structure spectroscopy. *Phys. Chem. Miner.* **25,** 323–327 (1998).
40. Jayasuriya, K., O'Neill, H. S. C., Berry, A. J. & Campbell, S. J. A Mössbauer study of the oxidation state of Fe in silicate melts. *Am. Mineral.* **89,** 1597–1609 (2004).
41. Jarrige, I., Cai, Y. Q., Ishii, H., Hiraoka, N. & Bleuzen, A. Thermally activated charge transfer in a Prussian blue derivative probed by resonant inelastic x-ray scattering. *Appl. Phys. Lett.* **93,** 054101 (2008).